JOURNAL OF GEOPHYSICAL RESEARCH, VOL. 112, B11301, doi:10.1029/2007JB005059, 2007

Click Here for Full Article

Source locations of secondary microseisms in western Europe: Evidence for both coastal and pelagic sources

S. Chevrot,[1] M. Sylvander,[1] S. Benahmed,[1] C. Ponsolles,[1] J. M. Lefèvre,[2] and D. Paradis[2]

Received 20 March 2007; revised 12 June 2007; accepted 20 July 2007; published 1 November 2007.

[1] We locate the sources of double-frequency (or secondary) microseisms in western Europe by frequency slowness analysis of array data as well as polarization and amplitude analysis at individual stations. Array analysis uses data recorded by a temporary array of broadband stations that we deployed in the Quercy region (southwest of France) and those from the Gräfenberg array, from 2 December 2005 to 30 January 2006. We determine attenuation laws for microseisms generated in the Mediterranean Sea and in the Atlantic Ocean, which allow us to use noise amplitudes to estimate distances from the source. We then combine azimuth and amplitude measurements to obtain precise locations of microseisms and estimate their source dimensions. Most of the time, microseismic noise originates in coastal regions where the swell reaches steep rocky coasts with normal incidence, in good agreement with the Longuet-Higgins model for the generation of secondary microseisms. In addition, we find evidence of occasional pelagic sources, which are closely related to moving storms, suggesting that nonlinear interaction between wave components can also generate secondary microseisms.

Citation: Chevrot, S., M. Sylvander, S. Benahmed, C. Ponsolles, J. M. Lefèvre, and D. Paradis (2007), Source locations of secondary microseisms in western Europe: Evidence for both coastal and pelagic sources, *J. Geophys. Res.*, *112*, B11301, doi:10.1029/2007JB005059.

1. Introduction

[2] Ocean gravity waves generate the continuous background signals between 0.05 and 0.3 Hz that are recorded by inland seismographic stations. Primary microseisms are generated in shallow water and produce a moderate peak in the 0.05–0.1 Hz frequency band (Figure 1). This peak is also found in ocean wave spectra, suggesting that primary microseisms are closely related to ocean swell [*Haubrich et al.*, 1963], and result from the interaction of ocean gravity waves with the shallow sloping seafloor or from the breaking of waves on the shore [*Hasselmann*, 1963]. Secondary or double-frequency microseisms (DFM) produce a much stronger peak in the 0.1–0.3 Hz frequency range (Figure 1), usually at a frequency that is twice the frequency of primary microseisms, suggesting that they are also produced in the oceans. While the mechanism for their generation has not yet been completely elucidated, they are thought to result from the nonlinear interaction of ocean gravity waves propagating in nearly opposite directions, an occurrence which produces standing waves that are coupled to the seafloor [*Longuet-Higgins*, 1950]. Locating the sources of secondary microseisms is important to identify "quiet" continental and ocean bottom recording sites. Because microseisms can be used for climate reconstructions from ocean waves [*Grevemeyer et al.*, 2000; *Bromirski and Duennebier*, 2002; *Essen et al.*, 2003], it is also important to identify the sources of microseisms and find the transfer functions that would allow us to reconstruct significant wave heights in the generation area from seismic records.

[3] Array analysis [e.g., *Friedrich et al.* 1998] and polarization analysis [e.g., *Schulte-Pelkum et al.*, 2004] of secondary microseisms have shown that at a particular location a small number of sources are visible and that these sources are stable over long periods of time (from a few days to a few weeks). Since microseisms are produced by swell near the shore line, and because this meteorological forcing is strongly spatially and temporally variable, the spatial and temporal stability of DFM sources is quite puzzling.

[4] Earthquakes are generally brief events with a well-defined origin time. Hence they produce transient waves that can be easily identified and picked. On the other hand, sources of DFM are continuously active and it is usually impossible to identify coherent arrivals in noise records. Therefore locating the sources of DFM requires different techniques than the ones classically used for locating earthquakes.

[1] Dynamique Terrestrie et Planétaire, UMP 5562, Observatoire Midi-Pyrénées, Université Paul Sabatier, Toulouse, France.
[2] Météo-France, Marine and Oceanographic Section, Toulouse, France.

0148-0227/07/2007JB005059$09.00

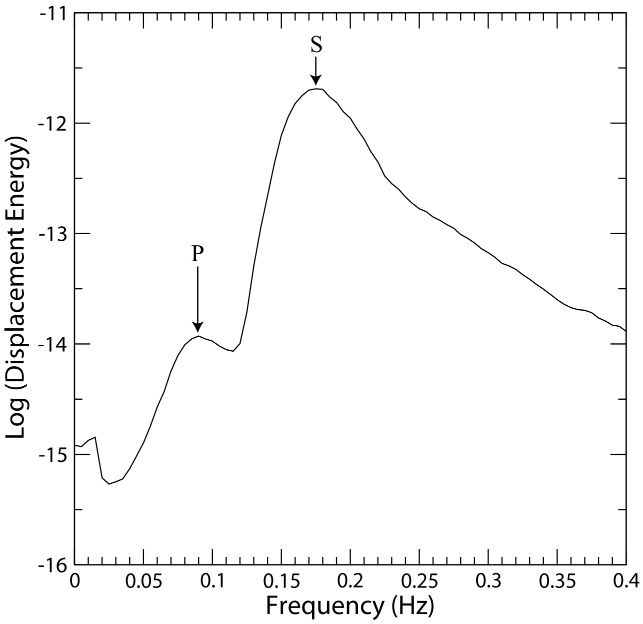

Figure 1. Average energy spectrum of displacement at station SSB (Figure 2) showing primary microseism (P) at a frequency of about 0.09 Hz and secondary microseisms (S) at a frequency of about 0.18 Hz. Note the 2:1 ratio between the frequency of secondary and primary microseisms.

[5] Different approaches have been used to locate the generation areas of microseismic energy. Early attempts tried to locate DFM sources by triangulation using two tripartite arrays of stations [*Ramirez*, 1940]. More recently, denser arrays of broadband stations, such as the NORSAR (Norway), GRF (Germany) or Large Aperture Seismic Array (LASA) (North America) arrays, have been used [*Cessaro*, 1994; *Friedrich et al.*, 1998; *Essen et al.*, 2003], but the localization precision remained rather poor. The amplitude of DFM can also be used to locate the sources of DFM [e.g., *Tabulevich et al.*, 1990]. The idea is to first derive an attenuation law of DFM which gives the variations of amplitudes with distance from the source and then use the amplitudes measured at different stations corrected for attenuation to locate the sources. Correlation between the amplitude of microseisms and ocean wave height models [*Essen et al.*, 2003] has been attempted, but this method is also characterized by poor spatial and temporal resolution. More recently, *Schulte-Pelkum et al.* [2004] have shown that noise polarization constrains the incoming direction of microseisms at a particular station, but they did not try to use it for source location. Finally, *Stehly et al.* [2006] used the antisymmetry of Green's functions obtained by correlating noise recorded by pairs of stations in North America and Europe to determine the incoming direction of primary and secondary microseisms. Their method revealed that primary microseisms have a seasonal variability, with sources located in the northern

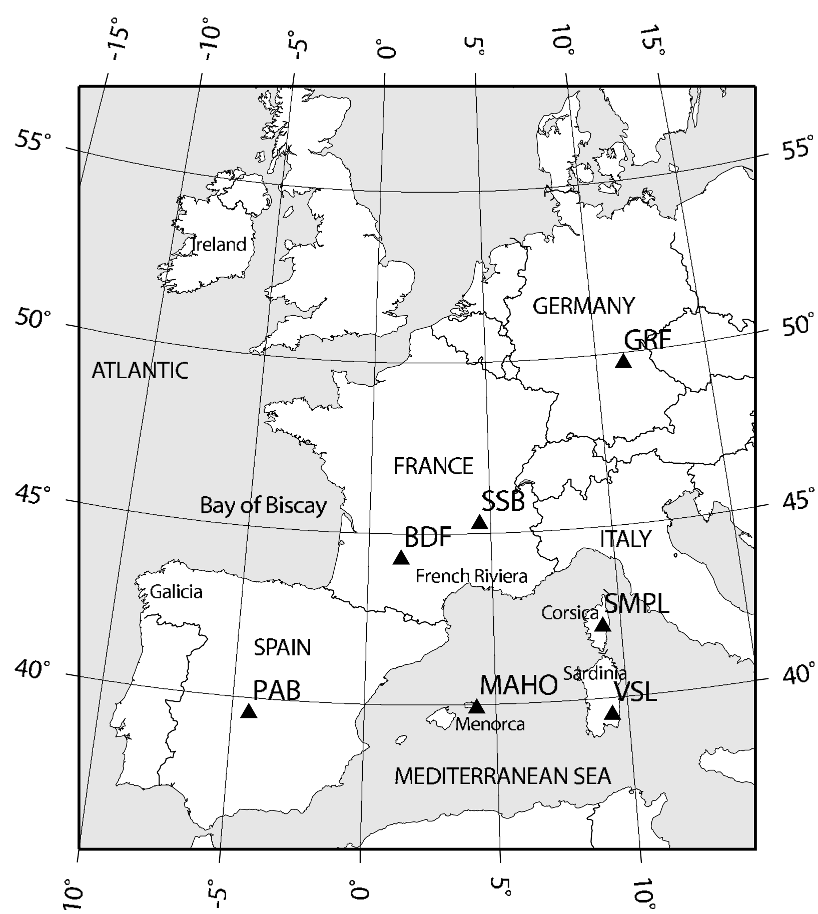

Figure 2. Location of individual broadband stations and arrays (BDF and GRF).

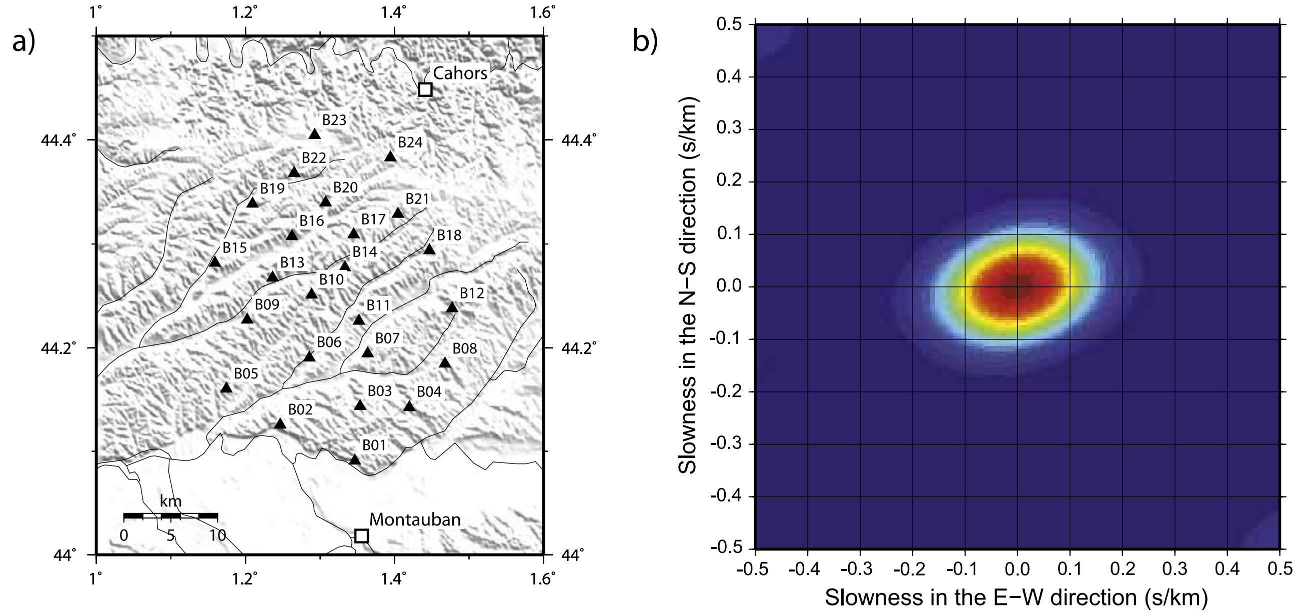

Figure 3. (a) Geometry of the Quercy array, composed of 24 broadband stations, deployed with a station spacing of about 5 km. (b) Slowness response of the Quercy array at a period of 6 s.

Atlantic and northern Pacific during winter, and in the southern Pacific during summer.

[6] Source localization of DFM gave contrasted results, with some studies revealing generation areas localized near the coastline [e.g., *Bromirski and Duennebier*, 2002] and others finding evidence of generation areas closely related to storm tracks in the deep ocean [e.g., *Cessaro*, 1994; *Tabulevich et al.*, 1990]. As a consequence, the understanding of the processes generating DFM has been hampered by a poor knowledge of both geometry and location of the sources of DFM. In this study, we combine frequency slowness analysis at arrays of broadband stations with polarization and amplitude measurements at individual stations in western Europe, to locate the sources of DFM in the Atlantic Ocean and in the Mediterranean Sea, with a much higher precision than in previous studies. We then compare our locations with wave height models and demonstrate that DFM are produced most of the time near the shore, in regions where the swell hits rocky coasts at normal incidence. However, we also find evidence of occasional pelagic sources that closely follow the trajectory of storms in the Mediterranean Sea.

2. Data and Processing

2.1. Quercy Array

2.1.1. Description of the Array

[7] From 2 December 2005 to 30 January 2006, we deployed an array of 24 broadband stations in the Quercy region (label BDF in Figure 2). This location was chosen so that we could observe both Atlantic and Mediterranean sources of microseisms, and because crustal structure under the array is rather simple. The geometry of the array is shown in Figure 3a. The array was composed of 14 Guralp CMG40 and 10 Chinese CDJ short-period seismometers, with bandwidth extended up to 20 s period. The Agecodagis Minititan stations recorded continuously, at a sampling rate of 31.25 Hz. Initially, the array geometry was designed to optimize the detection of secondary microseisms coming from the Bay of Biscay, with a larger aperture in the N-S direction (40 km) than in the E-W direction (30 km). We sought a regular array with a spacing of about 5 km between stations. The wavelength of DFM at 6 s being about 20 km, this spacing gives us a few samples per wavelength of the microseismic waves in the array response.

2.1.2. Array Response

[8] The slowness array response

$$R(\omega, \mathbf{p}) = |\sum_{n=1}^{N} e^{-i\omega \mathbf{p}\cdot\mathbf{r_n}}|^2, \qquad (1)$$

where ω is the frequency, $\mathbf{p}$ the slowness vector, and $\mathbf{r_n}$ the positions of the stations, is shown in Figure 3b, for a period of 6 s, typical for DFM recorded in southern France. The array response is very simple, with a unique principal lobe slightly larger in the E-W direction than in the N-S direction. Note the absence of secondary lobes, showing that this array is particularly well suited for the analysis of DFM, as expected.

2.1.3. Temporal Variations of DFM

[9] Data are first deconvolved from station responses and resampled at 5 Hz. Power spectra are then computed over nonoverlapping 200-s sliding windows. For each window, we compute the median of the power spectra for the different stations. The spectrogram is then obtained by taking the median of the power spectra every 6 h.

[10] The spectrogram for the Quercy array is shown in Figure 4a. Large earthquakes (magnitudes larger than 6.3) have a well-defined signature characterized by a vertical streak of high energy over a wide frequency band. For example, the band observed during 5 December (day 4 of

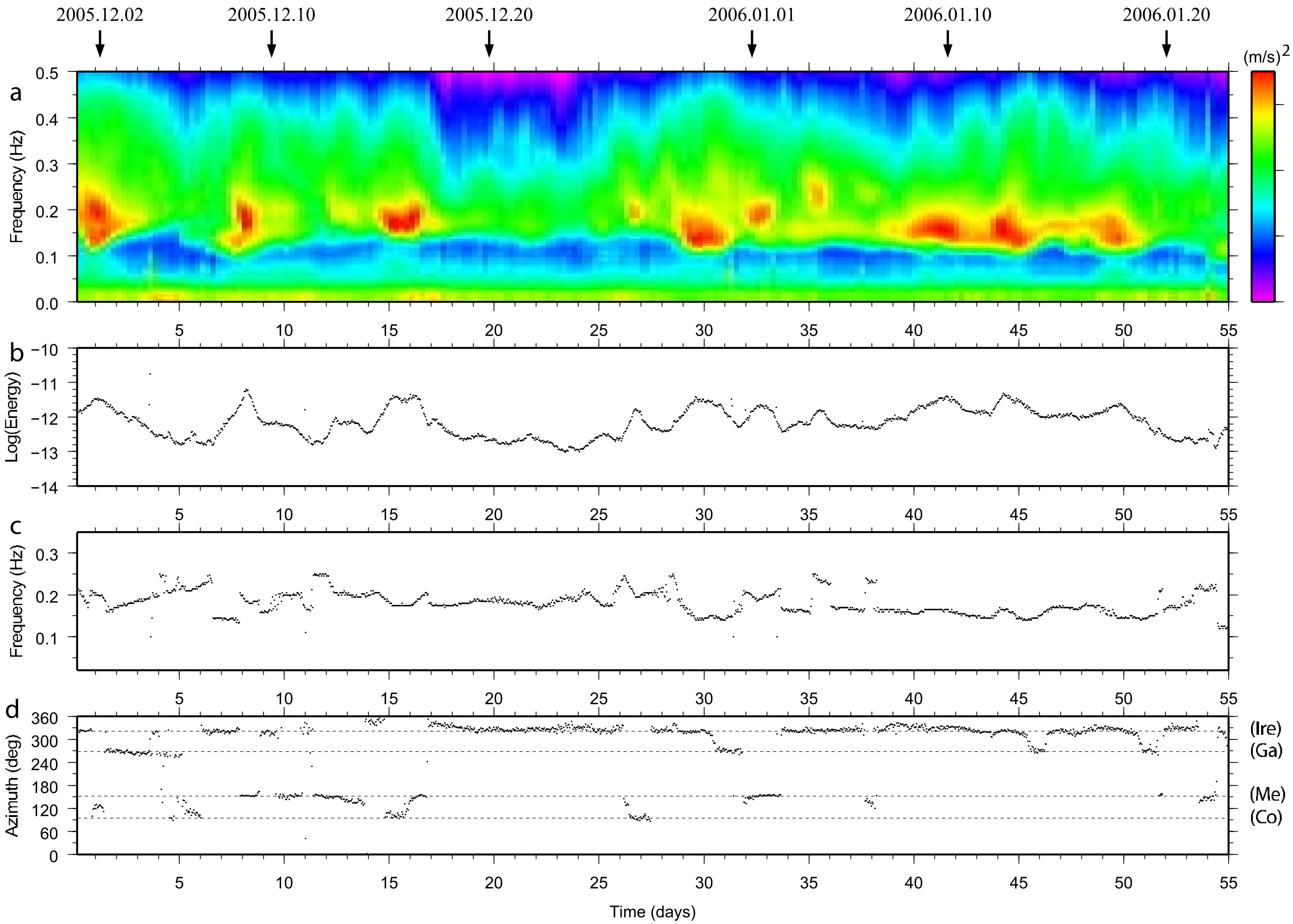

Figure 4. (a) Median spectrogram of vertical component data recorded by the Quercy array (BDF) from 2 December 2005 to 26 January 2006. (b) Logarithm of the energy of secondary microseisms. (c) Frequency of secondary microseisms. (d) Incoming azimuth of secondary microseisms. The four principal sources of microseisms seen by the Quercy array are located close to Ireland (Ire), Galicia (Ga), Menorca (Me), and Corsica (Co).

the experiment) corresponds to a magnitude 7.2 earthquake in Lake Tanganyika.

[11] For each time window, we determine the energy and frequency of the DFM peak between 0.1 and 0.5 Hz (Figure 4). Frequency slowness spectra are also computed over non-overlapping 200 s sliding time windows. The slowness sampling interval is 0.1 s/km in both the E-W and N-S directions. The data are filtered by a second-order band-pass Butterworth filter centered on the dominant frequency f_0 of DFM in the current window. The bandwidth of the filter is $f_0/5$. Slowness and azimuth of the incoming wave are determined from the position of the main beam in the frequency slowness spectrum:

$$S(\omega, \mathbf{p}) = |\sum_{n=1}^{N} A_i(\omega) e^{-i\omega \mathbf{p}\cdot\mathbf{r_n}}|^2, \quad (2)$$

where the $A_n(\omega)$ are the Fourier transforms of noise records at station n and frequency ω. Since microseisms produce mainly Rayleigh waves [e.g., *Tanimoto et al.*, 2006], we keep only measurements with slownesses in the range 0.25–0.36 s/km, corresponding to Rayleigh waves. Different sources of DFM can be active simultaneously. For example, from 2 December to 4 December (days 1 to 3 of the experiment), two distinct patches of energy are clearly identified in the spectrogram, corresponding to sources in the North Atlantic Ocean and in the Mediterranean Sea.

[12] Raw azimuth measurements show a large amount of scatter which we tried to reduce by using different filters and length of time windows, without success. To obtain more robust and stable azimuth measurements, we compute the median of the angles over 1 h intervals, following the method introduced by *Nikolaidis and Pitas* [1998]. The median of a set of measured angles ϕ_i is the angle ϕ_0 which minimizes the dispersion d, defined by

$$d = \frac{1}{N} \sum_{i=1}^{N} arc(\phi_i, \phi_0), \quad (3)$$

where $arc(\phi_i, \phi_0)$ is the smallest angle between ϕ_0 and ϕ_i:

$$arc(\phi_i, \phi_0) = 180 - |180 - |\phi_i - \phi_0||. \quad (4)$$

All the angles are defined between 0° and 360°. The median filtering dramatically reduces the scatter of azimuth measurements (Figure 4d).

[13] The distribution of azimuths is not random. They are concentrated in three distinct azimuthal bands. The first band ranges from 80° to 160°. This group, which corresponds to storms in the Mediterranean Sea, shows the strongest spatial and temporal variability. For example, the storm that began 17 December (day 16) at an azimuth around 90° moved to an azimuth of 160° 2 d later. The displacement of the apparent source of DFM on the Mediterranean Sea is also accompanied by strong amplitude variations. The second azimuth band lies in the range 250°–290° and corresponds to sources in the Bay of Biscay. The last group covers azimuths from 310° to 350°, pointing toward sources in the northern Atlantic.

[14] In the 0.1–0.5 Hz frequency band, two families of high-energy spectral patterns can be identified. The first pattern is characterized by DFM peaks moving in the direction of increasing frequency. For example, during 3–8 December 2005 (days 2 to 7), variations in the dominant frequency show a clear linear trend in both the spectrogram and the plot showing the variations in dominant frequency with time. This progressive frequency shift can be explained by the dispersion of ocean waves generated by distant storms in the Atlantic Ocean [*Haubrich et al.*, 1963]. This inference is confirmed by the frequency slowness analysis which finds that DFM are coming from the west of the array.

[15] Gravity waves propagating in deep water have a group velocity

$$U = \frac{g}{4\pi f} \quad (5)$$

so that long-period waves propagate faster than shorter period waves. If the source is not moving, the dominant frequency of the incoming swell increases linearly with time [*Haubrich et al.*, 1963]:

$$f = \frac{g}{4\pi r} t. \quad (6)$$

The distance r from the source can be estimated from the slope of $f(t)$, and the origin time, from the intercept time. For example, the linear trend in the spectrogram observed during 3 December (day 2) corresponds to a storm in the North Atlantic located approximately 1700 km from the coast.

[16] The second pattern, which is characterized by slightly higher-frequency peaks, corresponds to DFM events which have dominant frequencies decreasing with time. As suggested by the azimuths determined from array analysis (Figure 4d), these patterns correspond to storms developing in the Mediterranean Sea. Waves on a surface of water are produced by wind stress, which is proportional to the square of the wind speed. Significant wave height is determined by wind speed, wind duration, and fetch. As a storm develops, the height and dominant period of the sea waves increase. The second pattern is thus generated by swells produced locally by storms close to the shore where the nonlinear wave interaction producing DFM occurs. The best example of this second pattern is observed in the time interval 16–17 December 2005, when a strong storm developed in the Mediterranean Sea. This storm and its temporal evolution will be described below in more detail.

[17] Most of the time, the temporal evolution of the dominant frequency is less clear, and the only robust criterion to identify the DFM source region is the incoming azimuth. The strong spatial and temporal variability of DFM sources seen in this preliminary analysis results from simultaneous contributions of a variety of sources in the Atlantic Ocean and the Mediterranean Sea. Consequently, characterizing DFM in western Europe is more complicated than in regions with a single a simple coastline such as California, where DFM are mainly generated by swells produced by distant storms in the Pacific reaching the coast.

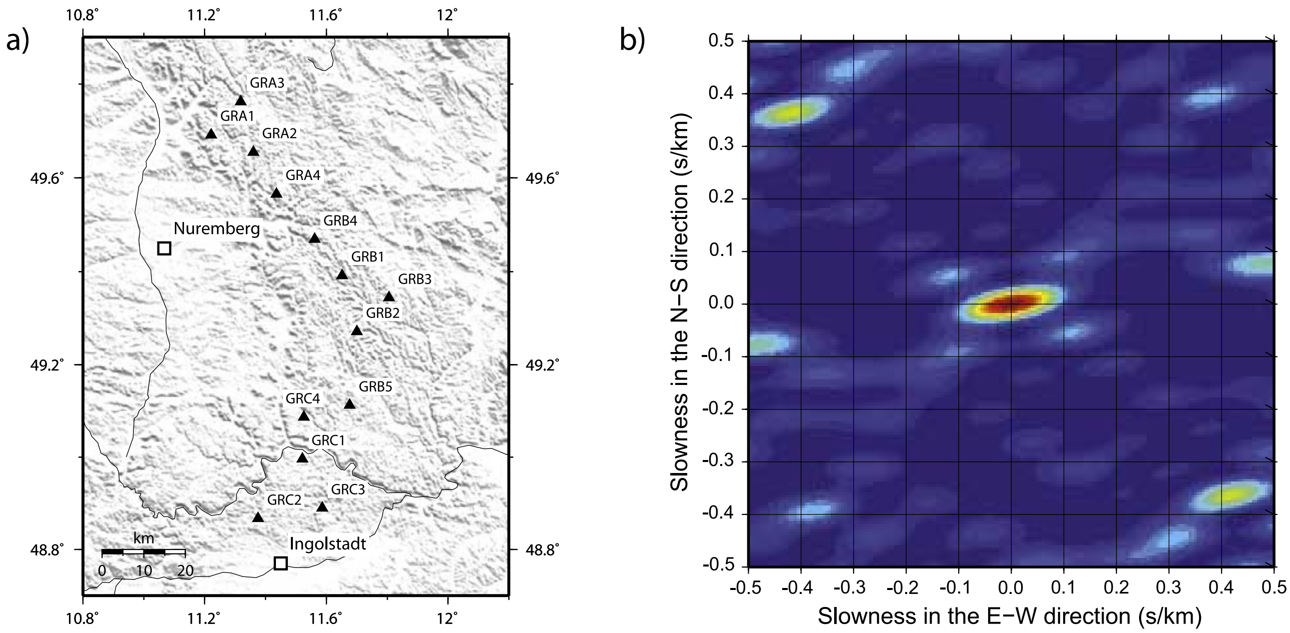

Figure 5. (a) Geometry of the Gräfenberg array, composed of 13 broadband stations, deployed with a station spacing of about 20 km. (b) Slowness response of the Gräfenberg array at 6 s period.

2.2. GRF Array

2.2.1. Description of the Array

[18] The Gräfenberg array (Figure 5a) is located in southeast Germany and is composed of 10 vertical and 3 three-component stations equipped with STS-1 seismometers. The average interstation distance of about 20 km is suitable for the analysis of DFM. In a previous study, *Friedrich et al.* [1998] used this array to locate the sources of primary and secondary microseisms over a four months period during winter 1995/1996.

2.2.2. Array Response

[19] The slowness array response of the Gräfenberg array is shown in Figure 5b, for a period of 6 s. Owing to a much larger aperture ($\sim$100 km) than the Quercy array, the main lobe is much smaller. However, because the interstation distance is of the same order of magnitude as the wavelength of Rayleigh waves at 6-s period, the array response shows multiple secondary lobes (Figure 5b) that complicate the determination of azimuths. As for the Quercy array, we consider only peaks corresponding to slownesses between 0.25 and 0.36 s/km, which allows us to identify the beams corresponding to DFM arrivals in the frequency slowness diagrams.

2.2.3. Example of Frequency Slowness Analysis

[20] Figure 6a shows the noise recorded by the stations of the Gräfenberg array around 1800 UT 17 December (day 16). The results of frequency slowness analysis on these data is shown in Figure 6b. While no coherent wave arrival can be seen on the records, array analysis clearly finds two coherent plane wave arrivals. The more energetic beam, at

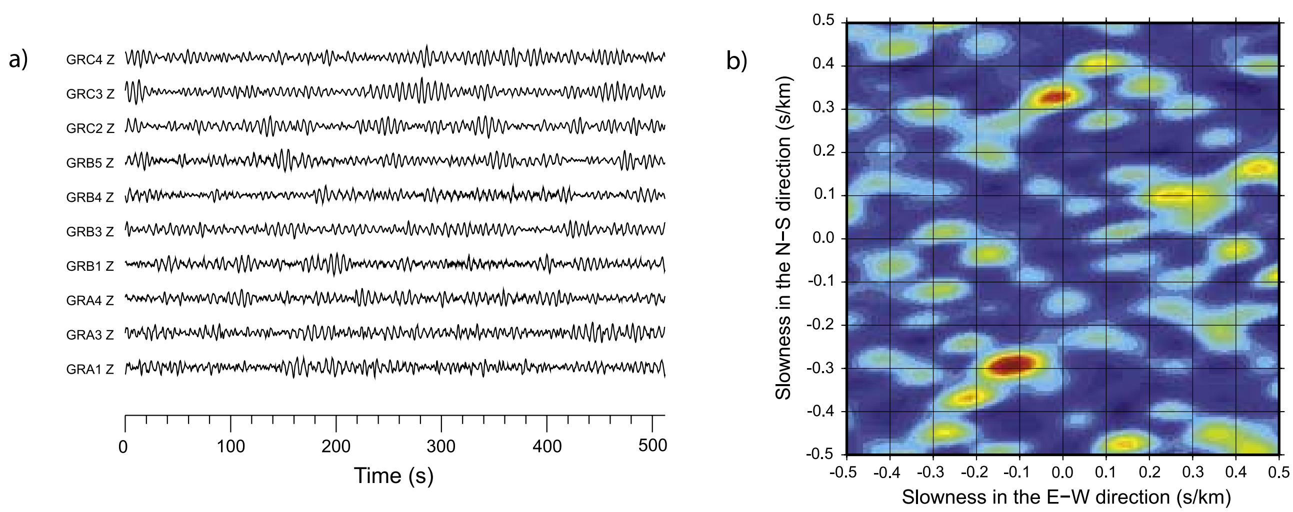

Figure 6. (a) Noise recorded by the stations of the Gräfenberg array around 1800 UT 17 December. (b) Corresponding frequency slowness diagram for band-pass-filtered data around 6 s.

an azimuth of about 200°, is produced by waves coming from the Mediterranean Sea. Such observations of simultaneously active multiple sources of DFM is quite common. In this example, the energy of the main beam represents about 35% of the total energy, which is a lower bound because the wavefront distortions will introduce deviations from the planar wave assumption. Even though different sources of DFM may be active simultaneously, noise records are usually strongly dominated by a single source which, as will be shown below, can be located precisely.

2.2.4. Temporal Variations of DFM

[21] We follow the same processing technique as for the Quercy array data. The results of frequency slowness analysis and the temporal evolutions of the amplitude and frequency of DFM are shown in Figure 7. The spectrogram for the GRF array (Figure 7a) is very similar to the one for the Quercy array (Figure 4a). Owing to the excellent sensitivity of STS-1 seismometers at long period, the primary microseisms are more clearly visible than on the Quercy array, with a well-defined 2:1 ratio between the frequencies of primary and secondary microseisms. In addition, bursts of energy are detected at very long period ($T > 50$ s), forming events that can last for a few days, with a very different signature from that of earthquakes. These long-period noise events follow similar temporal variations as the primary and secondary microseisms, suggesting a common origin for noise in the different frequency bands.

[22] The strong DFM amplitudes recorded between 9 January (day 39) and 22 January (day 52) are seen by both arrays. However, larger amplitudes are observed at the Gräfenberg array, with a higher frequency content. This suggests a generation area in the northern Atlantic, in good agreement with measured azimuths, which explains the stronger attenuation of DFM recorded at the Quercy array resulting from a much longer propagation distance. In contrast, the high frequency patterns coming from the Mediterranean Sea identified in the spectrogram of the Quercy array, for example during 10 December (day 9) or 3 January (day 33), are much smaller at the Gräfenberg array, or even absent. Finally, the Gräfenberg array detects large microseisms during 12 December (day 11), 15 December (day 14), and 23 January (day 53), which were not seen by the Quercy array. These events correspond to storms in the northern Atlantic and were probably too far from the Quercy array to be detected. Overall, the comparison of the results coming from the two arrays suggests that many sources of DFM are strong enough to produce identifiable signals at very distant stations, and thus should be straightforward to locate.

[23] As for the Quercy array, the azimuths determined with the GRF array are concentrated into a finite number of azimuthal bands, which are in good agreement with the ones found by *Friedrich et al.* [1998] between October 1995 and January 1996. Note that owing to the median filter, our azimuth measurements show much less scatter than theirs.

[24] Combining the observed azimuths at the Quercy and Gräfenberg arrays should allow us to determine the location of the sources of DFM by triangulation. However, these arrays are sometimes dominated by different DFM because of their distant locations. In addition, using only two arrays is hardly sufficient to obtain precise locations. We have thus decided to include measurements of noise polarization at a number of permanent broadband stations to improve the localization of DFM sources.

2.3. Polarization Analysis at Individual Stations

[25] In addition to array data, we have analyzed the continuous LH channel (1 s sampling interval) of stations MAHO, PAB, SMPL, SSB, and VSL (see Figure 2) from 2 December 2005 to 31 January 2006.

[26] The particle motion of secondary microseisms, which are mainly composed of Rayleigh waves, is elliptical [e.g., *Tanimoto et al.*, 2006], and the polarization in the horizontal plane can be used to infer the incoming direction of microseisms at a particular station. The continuous records are cut into consecutive 200-s-long time windows. Inside each window, DFM frequency f_0 is determined from the largest peak observed in the power spectrum of the vertical component between 0.1 and 0.5 Hz. We use the frequency-dependent polarization method of *Park et al.* [1987] with 5 eigentapers to measure the azimuth of the principal horizontal polarization axis around frequency f_0. Fundamental mode Rayleigh waves have a retrograde particle motion at the surface. This property can be used to resolve the 180° ambiguity in azimuth and determine the true incoming directions. Because different arrivals of microseismic noise and teleseismic waves often interfere in the microseismic frequency band, polarization measurements are less robust than the measurements obtained from array analysis. Using longer time windows has little effect on the amount of scatter in polarization measurements. Thus we decided to use a rather short time window and then apply a median filter on the polarization directions, as for the azimuths measured by array analysis. In the end, we obtain a time series of DFM polarization directions with a sampling interval of 1 h. Our data processing technique gives more stable and robust results than the method used by *Schulte-Pelkum et al.* [2004].

[27] Figure 8 shows the results of polarization analysis for station SSB. For this permanent station, the azimuth measurements are almost as good as the ones obtained by array analysis. The other stations (not shown here) give measurements of similar quality.

3. Preliminary Localization of DFM Sources

[28] We first localized the DFM sources from the azimuths determined by array and polarization analysis. We explore all the possible locations of DFM by a systematic grid search and find the location which minimizes the misfit function

$$\chi^2(\mathbf{r}) = \sum_{i=1}^{N} \frac{[\text{arc } \phi_i, \phi(\mathbf{r})]}{\sigma_i^2}. \qquad (7)$$

The σ_i represent the errors in the azimuth measurements, which are 10° for array analysis and between 10° and 40° for single-station analysis. The amount of scatter in single-station azimuth measurements is highly variable, and depends on the quality of the horizontal components as well as on the distance to the DFM source. In a case where the source of DFM is just north of Menorca, station MAHO (Figure 2), which is only a few tens kilometers away, gives

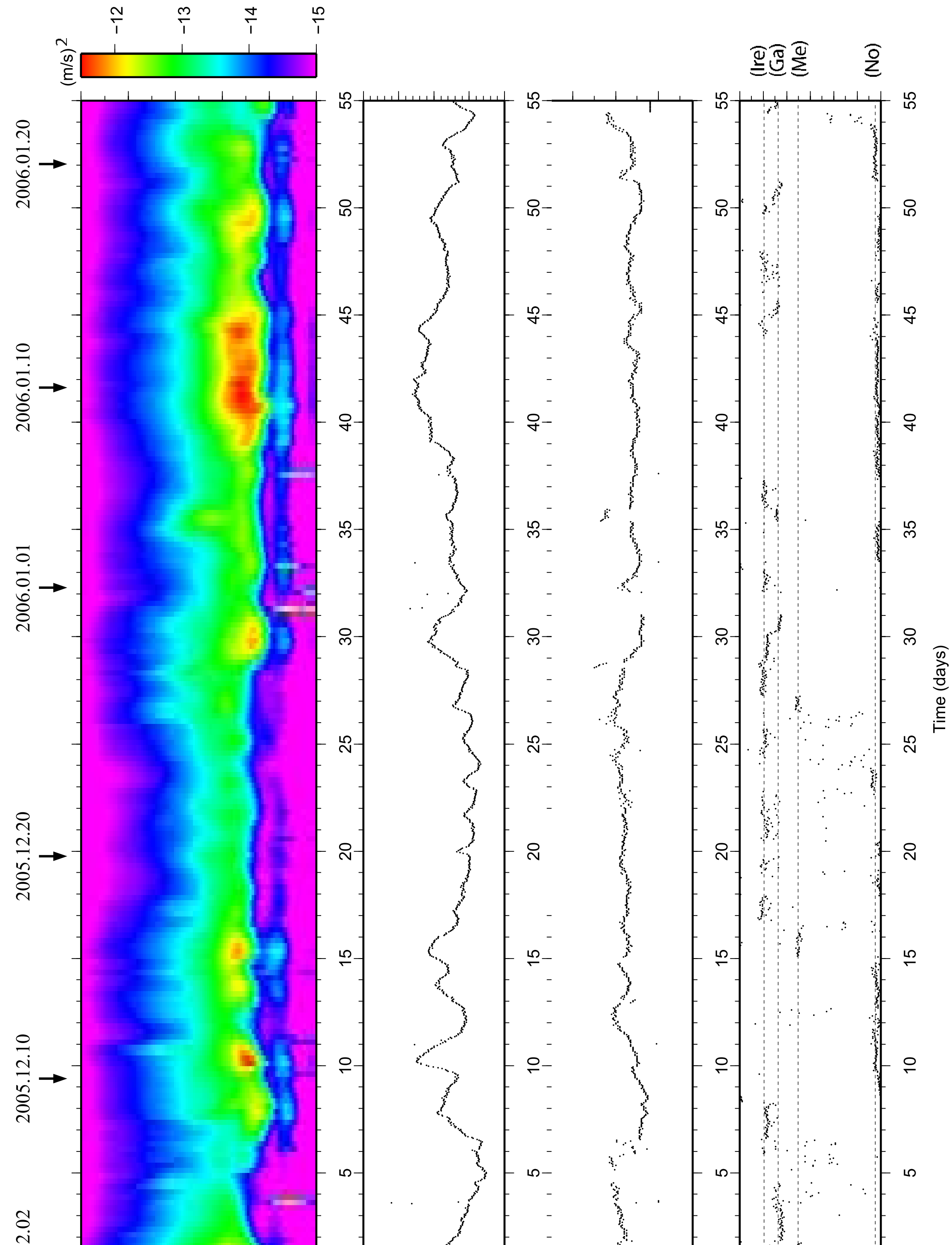

Figure 7. (a) Median spectrogram of vertical component data recorded by the Gräfenberg array (GRF) from 2 December 2005 to 26 January 2006. (b) Logarithm of the energy of secondary microseisms. (c) Frequency of secondary microseisms. (d) Incoming azimuth of secondary microseisms. The four principal sources of microseisms seen by the Gräfenberg array are located close to Ireland (Ire), Galicia (Ga), Menorca (Me), and in the Norwegian Sea (No).

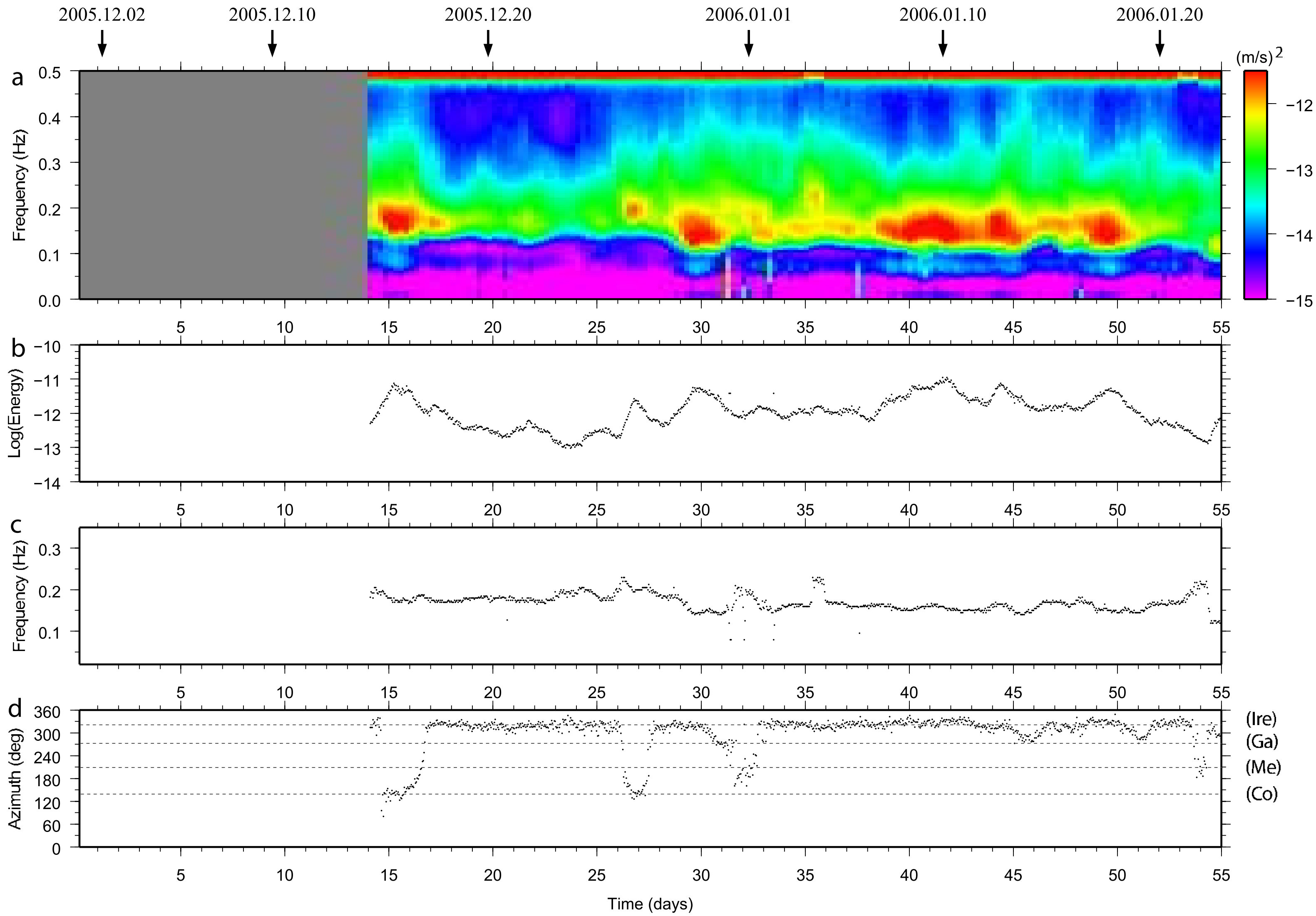

Figure 8. (a) Median spectrogram of vertical component data recorded by station SSB from 2 December 2005 to 26 January 2006. (b) Logarithm of the energy of secondary microseisms. (c) Frequency of secondary microseisms. (d) Incoming azimuth of secondary microseisms. The four principal sources of microseisms seen by station SSB are located close to Ireland (Ire), Galicia (Ga), Menorca (Me), and Corsica (Co).

azimuths that can vary by as much as 45°. The azimuths measured by array analysis are more stable and robust, so their lower errors give them a larger weight in the preliminary location. We keep stations that record secondary microseisms with the same frequency and for which the measured incoming directions point toward the same region. The summation is performed over the set of N arrays and stations which have seen the source. Very often, different DFM sources are active simultaneously and the different stations do not see the same predominant source during a given time interval. Consequently, the number of stations that can be used for this preliminary location typically varies between 3 and 7. The localization procedure is repeated every hour, for the whole duration of the experiment, and the source locations are stored in a catalog.

3.1. Attenuation Laws of Microseisms

[29] In a second step, we use the preliminary locations to determine the attenuation laws of double-frequency microseismic noise. We only consider the best locations, corresponding to the largest amplitudes of microseismic noise recorded by all the stations. The energy of noise at station i for source j in region k is given by

$$e_{ijk} = \frac{s_j r_i}{\Delta_{ij}} \exp\left[\left(-\frac{\omega_j}{cQ_k}\right)\Delta_{ij}\right], \tag{8}$$

where ω is the frequency, Δ_{ij} the distance to the source, r_i the site response at station i, s_j the source energy, c the phase velocity of Rayleigh waves, and Q_k the quality factor for microseisms generated in region k. Site response terms will absorb errors that may contaminate station responses. Frequency of DFM typically varies between 0.15 Hz and 0.25 Hz. Inside this frequency band, we assume a constant phase velocity of Rayleigh waves of 3.3 km/s. Taking the logarithm of (8) yields

$$E_{ijk} = R_i + S_j - \Delta_{ij} - \frac{\omega\gamma_k}{c}\Delta_{ij}, \tag{9}$$

where E_{ij} = log e_{ij}, R_i = log r_i, S_j = log s_j, $\gamma_k = 1/Q_k$. We solve this linear system of equations to determine site, source and propagation parameters simultaneously (R_i, S_j and attenuation parameters γ_k) with the constrain that the sum of the R_i terms is zero. We invert jointly the data for the three source regions that we identified after the preliminary locations: Mediterranean Sea (Menorca), North Galicia, and west coast of Ireland. Figure 9 displays the results of the inversion. After correction for site responses and energy of the different sources, the logarithm of the energy of DFM shows little scatter around the average attenuation laws (shown with black lines). The estimated quality factors are $Q = 521$ for North Galicia, $Q = 283$ for Ireland, and $Q = 191$ for Mediterranean Sea sources. Owing to poor distance distributions at each station, there is a trade-off between site responses and attenuation parameters. There is also a trade-off between attenuation parameters and source energies. Thus we should not pay too much attention to the particular values of the different parameters at this point. However, the solution gives a consistent set of parameters that allows us to predict a distance from the source from the observed level of noise at a particular station. This property will be exploited in section 3.2.

3.2. Localization Using Amplitudes

[30] In a final step, we combine amplitude and azimuth measurements to refine the locations of DFM sources. We now use the hourly medians of both azimuth and amplitude of DFM at each station to define location vectors $\mathbf{x_i}$, represented by points on the sphere. A location vector is defined by

$$\mathbf{x_i} = \left(\sin\theta_i^S \cos\phi_i^S, \sin\theta_i^S \sin\phi_i^S, \cos\theta_i^S\right), \tag{10}$$

where θ_i^S and φ_i^S are the spherical colatitude and longitude of the source seen by station i, respectively. These two angles can be determined from the incoming noise azimuth λ_i and from the angular distance to the source Δ_i, which is calculated from the amplitude of DFM at station i and the attenuation law corresponding to the source region. The colatitude of the source is given by the cosine formula

$$\cos\theta_i^S = \cos\Delta_i \cos\theta_i^R + \sin\theta_i^R \sin\Delta_i \cos\lambda_i, \tag{11}$$

and the longitude by the sine formula

$$\sin\left(\phi_i^S - \phi_i^R\right) = \sin\Delta_i \frac{\sin\lambda_i}{\sin\theta_i^S}, \tag{12}$$

where θ_i^R and ϕ_i^R are the colatitude and longitude of receiver i, respectively.

[31] The new source locations are given by the direction of the average of the location vectors

$$\mathbf{r} = \frac{1}{N}\sum_{i=1}^{N} \mathbf{x_i}. \tag{13}$$

Figure 10 shows the hourly location vectors for all the stations (color solid circles) and the average source location (star) for 17 December between 0300 and 0900 UT. In this time interval, the hourly location vectors at individual stations show little scatter. This suggests that the source area of DFM is limited in extent, much smaller than the area of the storm, and is not moving. On the other hand, location vectors for some stations seem to deviate systematically from the average source position. For example, the location vectors for station MAHO (orange circles in Figure 10) are all shifted to the south, but at about the correct distance from the station. This suggests that source mislocation results from a systematic deviation of the apparent incoming direction of DFM at station MAHO and not by complexity of DFM excitation in the source region. Whether Rayleigh waves are deviated from their great circle path by short-wavelength structures [*Woodhouse and Wong*, 1986] and/or by refraction at continental margins is still an open question. Accordingly, we can expect that better modeling of the

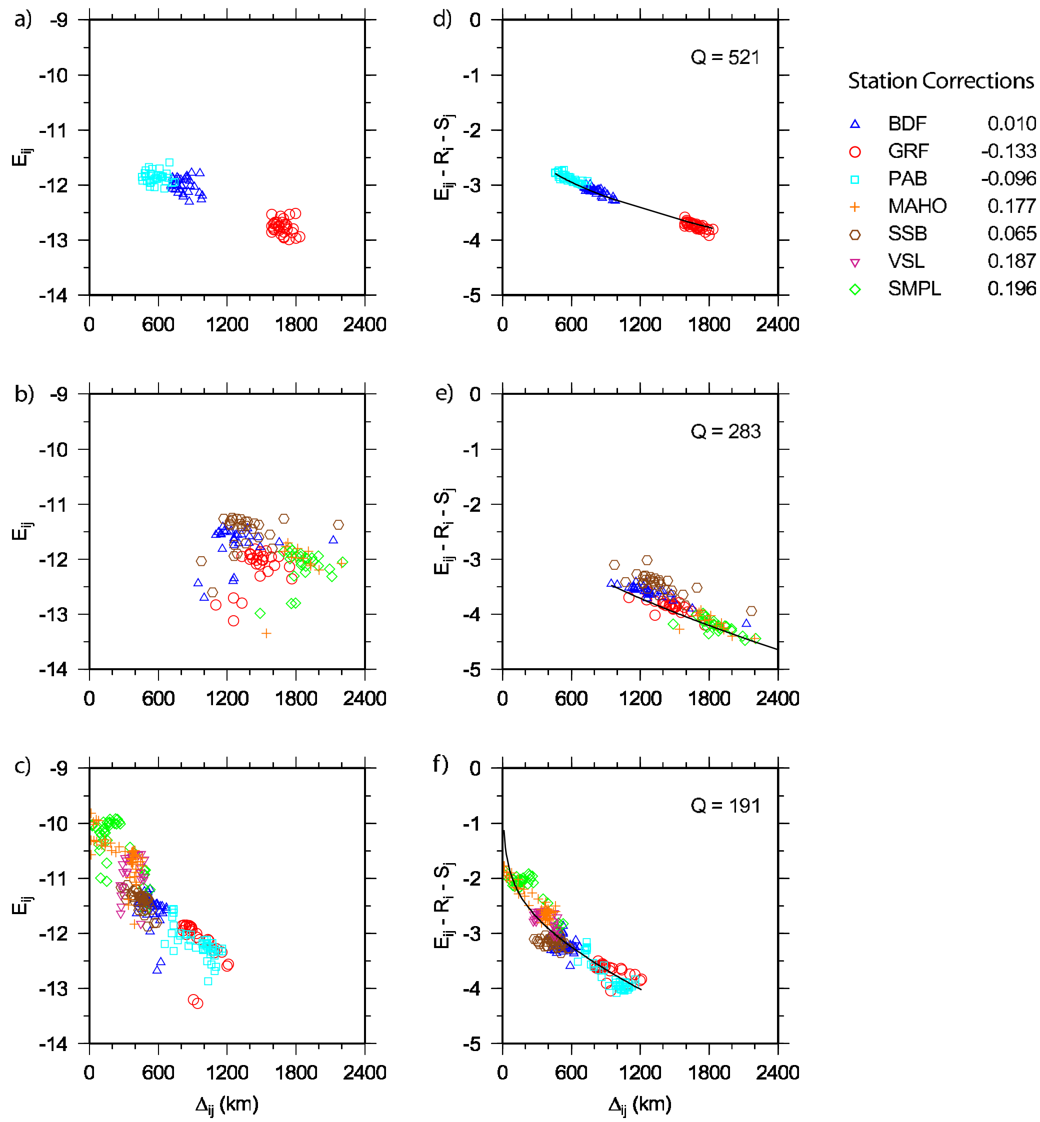

Figure 9. Observed energy of secondary microseisms as a function of distance from (a) the North Galicia, (b) west coast of Ireland, and (c) Mediterranean Sea sources. Variation of the energy of secondary microseisms as a function of distance after correction for site amplification and source energy for the (d) North Galicia, (e) west coast of Ireland, and (f) Mediterranean Sea sources. The attenuation laws for the three regions are shown by the solid black lines.

propagation of surface waves in heterogeneous continental and oceanic crusts will improve the precision of DFM localization. This possibility will be explored in subsequent studies.

4. Relation Between DFM Source Locations and Ocean Wave Heights

4.1. Description of the Sea Wave Model

[32] We consider a second-generation ocean surface wave model produced by Météo-France to predict sea states over the global ocean and over subareas with a higher spatial resolution. The wave model is obtained by a linear combination of the original VAG linear wind input term, the WAM (Wave prediction Model) exponential wind input term [*The Wamdi Group*, 1988; *Komen et al.*, 1994], and the WAM dissipation term [*Komen et al.*, 1994]. In a first step, the part of the wave spectrum corresponding to the wind sea is selected and the total energy of this domain is limited (if necessary) to the total energy of the Pierson-Moskowitz spectrum [*Pierson and Moskowitz*, 1964] which corresponds to the fully developed spectrum associated with the specified wind speed. This limitation allows us to work around of an imbalance between the growth and dissipation terms. In a second step, the wind sea part of the spectrum is reshaped according to a JONSWAP (Joint North Sea Wave Atmosphere Program) spectrum with a squared cosine distribution [e.g., *Hasselmann et al.*, 1980].

[33] The model is valid in shallow water outside the surf zone with a parameterization of bottom friction and percolation [*Shemdin et al.*, 1978]. Shoaling effects and angular

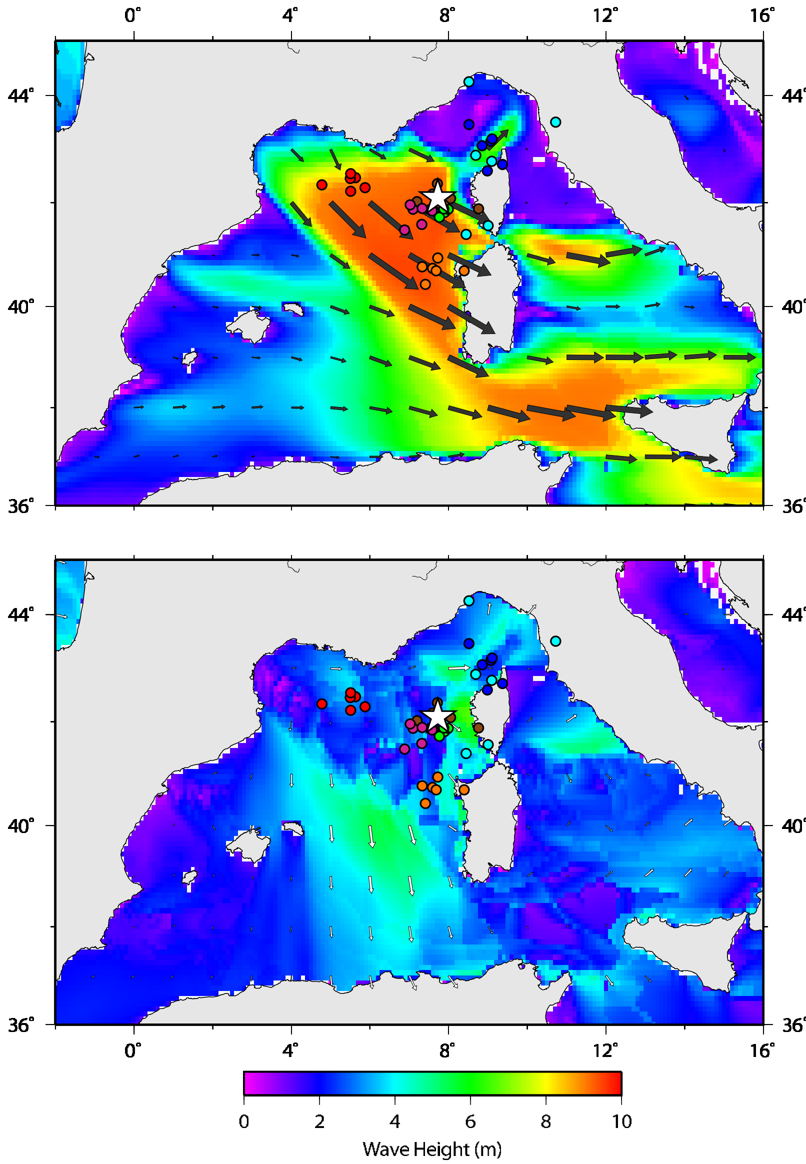

Figure 10. Snapshot of the wave model at 0600 UT 17 December 2005. (top) Significant wave heights of the wind sea and average wave propagation directions (black arrows). The white star shows the source location obtained by averaging the locations from stations GRF (red circles), BDF (blue circles), PAB (light blue circles), SMPL (green circles), SSB (brown circles), VSL (pink circles), and MAHO (orange circles). (bottom) Significant wave heights of the primary swell and wave average propagation directions (white arrows).

refraction can also be taken into account. The numerical scheme used for propagation is a first-order upwind flux scheme in spherical coordinates. The model is implemented at the global scale for up to 102 h for predictions at a resolution of 1 degree. A regional model is nested in the global model with a finer resolution of 0.25 degree to predict sea states around western Europe up to 54 h in advance. A fine resolution wave model driven by Aire Limitée Adaptation dynamique Développement International (ALADIN) winds is finally nested in the regional European sea model, covering the coasts of France with 54-h forecasts. The global wave model is implemented for deep waters, whereas in the fine resolution model, the bottom friction is also taken into account.

4.2. The 17–18 December Mediterranean Storm

[34] Of special interest is the 17–18 December Mediterranean storm during which the observed azimuths show unusually strong and rapid temporal variations (e.g., Figure 4). We reconstruct the detailed spatiotemporal distribution of DFM sources from the hourly measurements of amplitudes and azimuths (Figure 11).

[35] In the morning of 17 December (day 16), the location vectors consistently point toward a region about 100 km west of the coast of Corsica (Figure 10). While the region effected by the storm, with significant wave heights larger than 8 m, is rather extended, generation of DFM is limited to a very small area. Interestingly, this area is located close to the eastern limit of the strong wind sea (Figure 10, top).

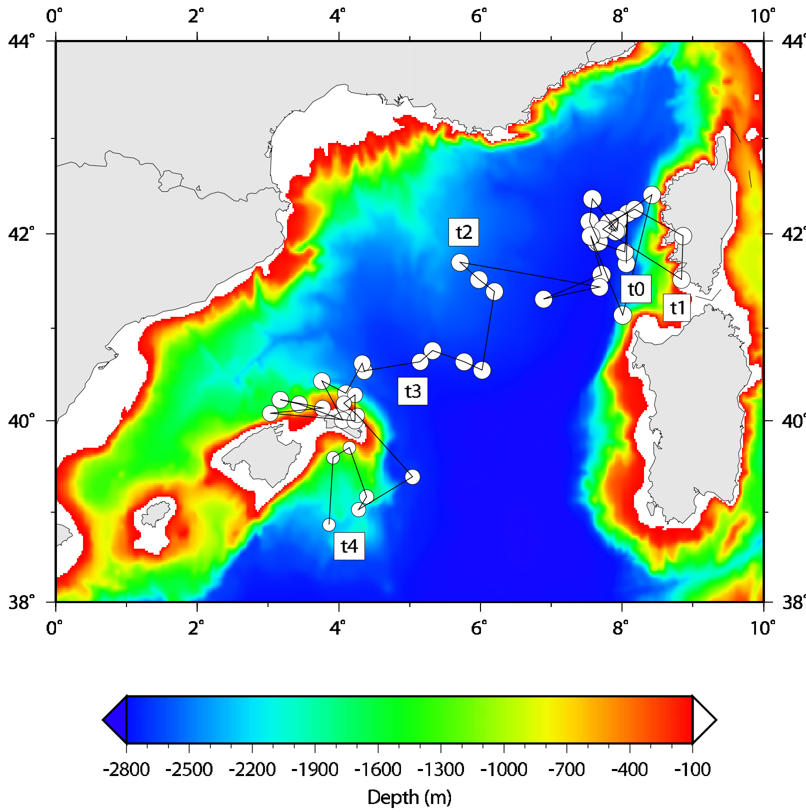

Figure 11. Trajectory of the source of secondary microseisms during the 17–18 December 2005 Mediterranean storm. The hourly position of the source is shown with white circles, between t0 = 0030 UT 17 December and t4 = 2330 UT 18 December. The other indicated dates are t1 = 1430 UT 17 December, t2 = 2230 UT 17 December and t3 = 0530 UT 18 December.

This limit corresponds to a strong gradient of significant wave height, with a sharp decrease toward the east. Further east, the primary swell component becomes dominant in the wave model (Figure 10, bottom). At 0000 UT 18 December (day 17), the dominant direction of the wind rotates rapidly toward the south. The source of DFM is moving rapidly toward the west, following the migration of the wind sea crossing the Mediterranean Sea (Figure 12). The location vectors are broadly distributed, suggesting an extended source, but more likely result from the large area that is hit by the rapidly moving storm during this 6-h observation time interval. The average location is in the trail of the moving storm, where the wind is strongly variable, and close to the limit between dominant wind sea and primary swell. In any case, the spatiotemporal correlation between the positions of the microseismic sources and the storm strongly suggests a causal link and a deep water origin for microseisms. At noon, the swell has reached the northern coast of Menorca Island, where we also locate the source of DFM (Figure 13). The amplitude of the swell then starts to slowly decrease and the storm ends around 18:00. The amplitude of microseisms follows a similar trend and vanishes at the end of the storm.

[36] The geometry of the storm system which produces DFM along the northern coast of Menorca during 18 December (Figure 13) is frequently encountered. In fact, it is the principal generation mechanism of microseisms in the Mediterranean Sea. It corresponds to a fetch of limited extent, going from the French Riviera to Menorca, generated by a southward blowing mistral. This rather small fetch explains why the dominant period of microseisms generated in the Mediterranean Sea is always smaller than the period of microseisms generated by stronger and broader storm systems in the Atlantic.

4.3. North Galicia Margin Sources

[37] Sources located near the North Galicia margin are less spatially variable than the Mediterranean sources. The former are found when strong swells produced by storms in the North Atlantic Basin reach the Bay of Biscay, for example during 4 December (Figure 14). While swell affects a broad coastal region from north of Portugal up to Brittany in France, the generation area of microseismic noise is again found limited to a very small region where waves reach the Galicia coast at nearly normal incidence. This is also the case along Vendée, for example, which does not seem to be an active source of DFM. However, while the coast of Vendée is gently dipping, with very long and flat sand beaches, the Galicia coast is characterized by steep rocky cliffs.

4.4. Other Sources

[38] With our limited data set, we have also found evidence for a strong source of DFM close to the western

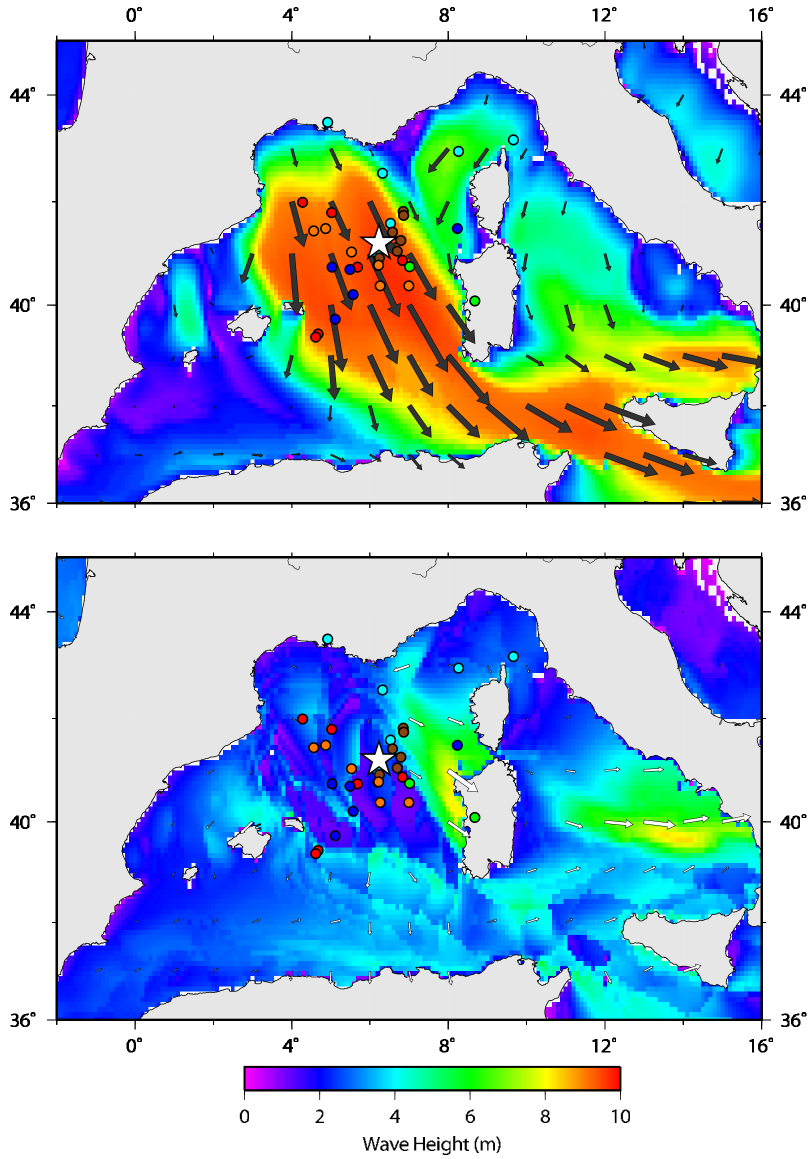

Figure 12. Same as Figure 10 but at 0000 UT 18 December 2005.

coast of Ireland (Figure 15). This source is again found in front of a very steep coastline, approximately perpendicular to the incoming swell direction. We also found some sources in the Norwegian Sea, which we could not locate precisely. Future studies considering a larger number of broadband stations, with an improved station distribution in northern Europe, should help us to put further constrains on the exact location of these sources.

5. Discussion

[39] We have shown that amplitude and azimuth measurements of DFM signals at a limited number of stations can be used to locate precisely their sources. While these locations may be improved by considering a larger number of stations, we have identified a fundamental limitation in locating DFM sources. Surface waves are deviated off their great circle plane by small-scale crustal heterogeneities and by refraction at continental margins or at major tectonic boundaries. These propagation effects will be investigated in a subsequent study in which we will model the propagation of surface waves inside the crustal model CRUST2.0 with a spectral element method.

[40] It has been shown that infrasounds and microseisms have a common origin in the ocean and that they follow similar temporal variations in amplitude and frequency [e.g., *Donn and Naini*, 1973; *Tabulevich et al.*, 1990; *Ponomaryov et al.*, 1998; *Willis et al.*, 2004]. Microbarometric observations could thus provide independent and complementary information to better locate the sources of noise. However, the incoming directions of microbarometers at infrasound arrays are affected by topographic shadowing and atmospheric winds [*Willis et al.*, 2004; *Garcés et al.*, 2004], which complicates their interpretation. We thus did not consider this source of information in this (preliminary) study.

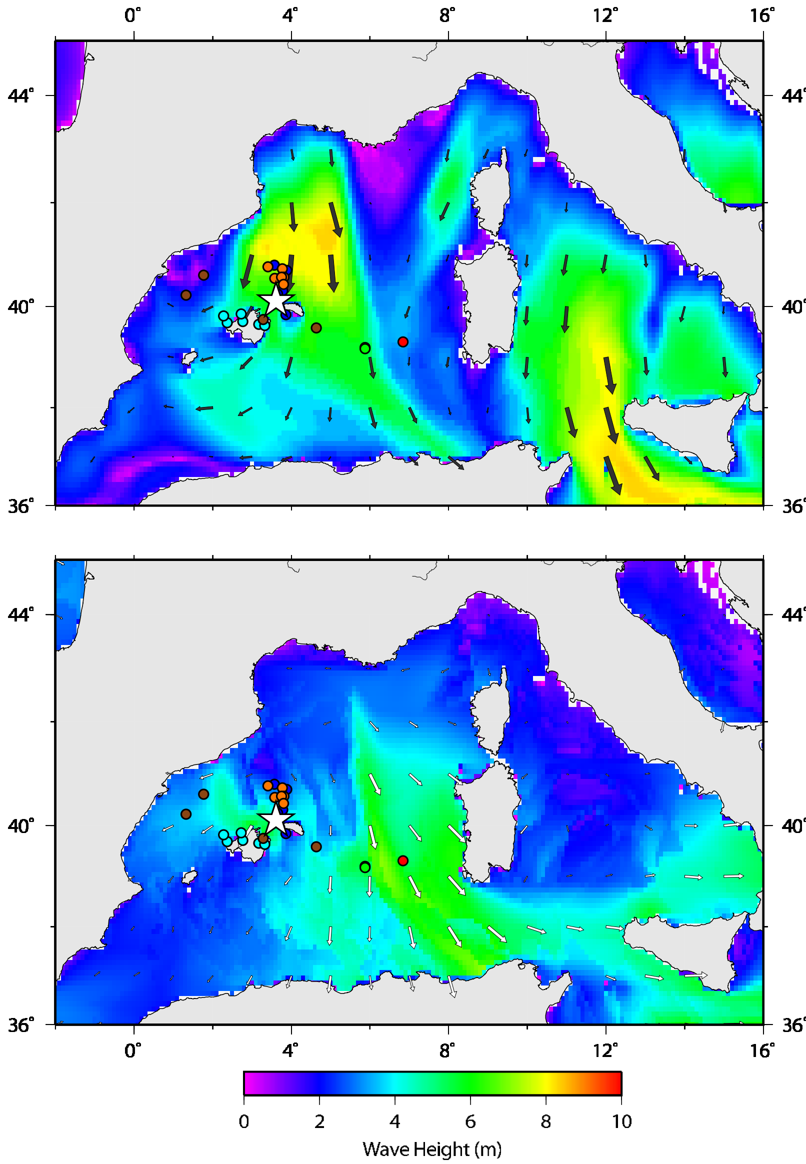

Figure 13. Same as Figure 10 but at 1200 UT 18 December 2005.

[41] The absence of DFM sources in the Bay of Biscay, where strong and extended storms occur frequently, is surprising. Its coastline is composed of gently dipping beaches in contrast to the steep rocky cliffs which characterize North Galicia, Menorca Island and the western coast of Ireland where the strongest sources of DFM are located. Thus it seems that the nature of the coast, which determines its ability to reflect the swell, may control DFM. Breaking or reflection of waves reaching the coast is of importance for engineers in charge of designing marine structures such as docks or sea walls. The problem is to quantify the forces exerted by breaking waves on these structures or the choppiness of the sea produced by interference between incident and partially reflected swell in front of a seaport. The first quantitative results on swell reflection by dipping surfaces were obtained by *Miche* [1944, 1951], a French marine engineer. The swell reflection coefficient depends on the inclination of the coast and on the wave slope γ, defined as the ratio between the wave height and the wavelength. The maximum value of γ corresponding to a swell that can be totally reflected by a plane of inclination α is given by [*Miche*, 1951]

$$\gamma_{\max} = \frac{\sin^2 \alpha}{\pi} \sqrt{\frac{2\alpha}{\pi}}. \tag{14}$$

The reflection coefficient is then given by

$$R = \frac{\gamma_{\max}}{\gamma}. \tag{15}$$

Values of $\gamma_{\max}$ decrease rapidly when the slope decreases, which explains the observation that high waves break over a gently dipping beach, but low waves are reflected. *Munk and Wimbush* [1969] have given a simple criterion governing the breaking of waves on shores. For a vertical displacement $\eta = a \cos \omega t$ the acceleration of the water line along the inclined bottom has the amplitude $\omega^2 a/\sin\ \alpha$.

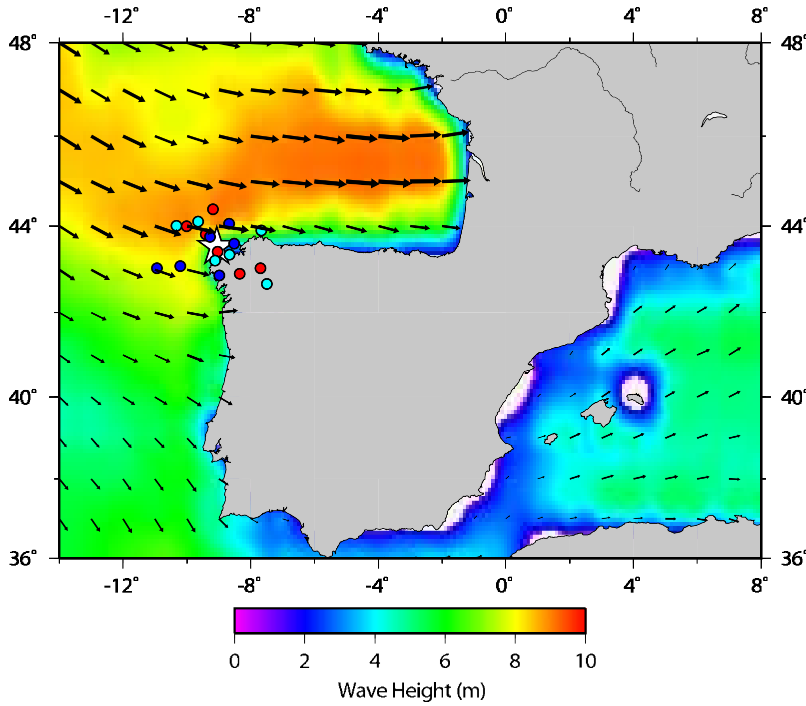

Figure 14. Significant wave height model (wind sea + primary swell) at 1200 UT 4 December. The white star shows the Galicia source location obtained by averaging location vectors from stations GRF (red circles), BDF (blue circles), and PAB (light blue circles). Average wave propagation directions are shown with black arrows, whose lengths are proportional to wave heights.

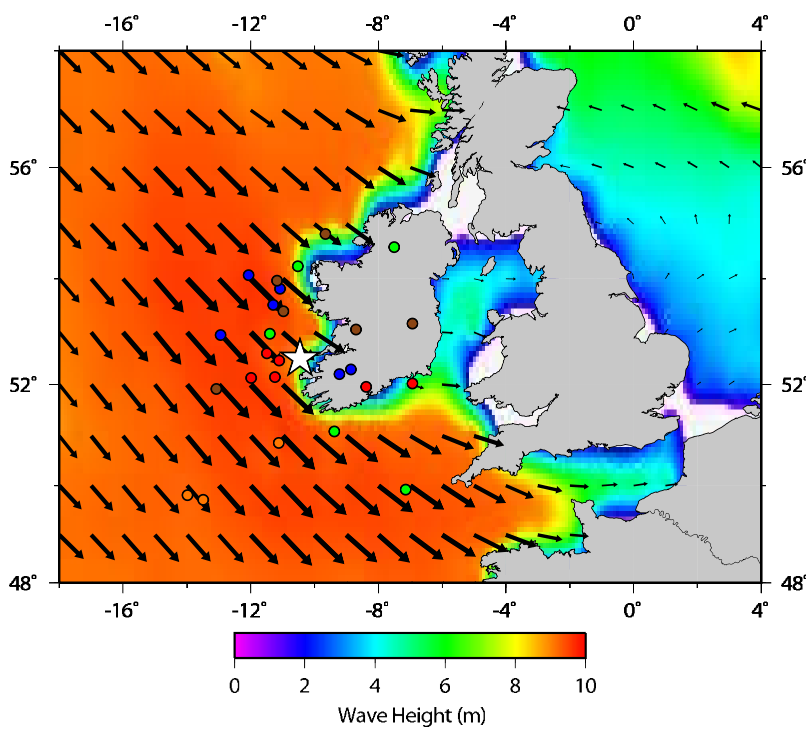

Figure 15. Significant wave height model (wind sea plus primary swell) at 0000 UT 1 January. The white star shows the western coast of Ireland source location obtained by averaging location vectors from stations GRF (red circles), BDF (blue circles), SMPL (green circles), SSB (brown circles). Average wave propagation directions are shown with black arrows, whose lengths are proportional to wave heights.

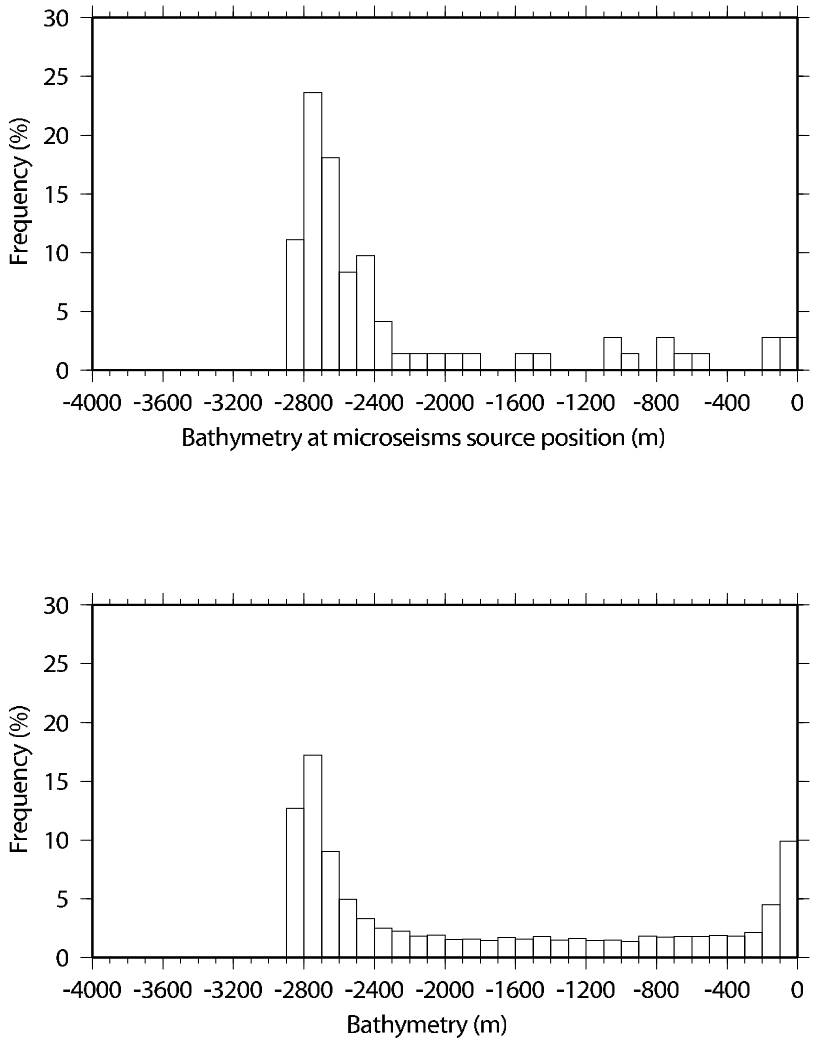

Figure 16. (top) Histogram of bathymetry at the location of secondary microseism sources in the Mediterranean Sea. (bottom) Histogram of bathymetry in the Mediterranean Sea.

Breaking occurs when this acceleration exceeds the downslope component of gravity $g \sin \alpha$, which defines a critical slope α_c

$$\sin^2 \alpha_c = \frac{\omega^2 a}{g}. \quad (16)$$

For small inclinations, this criterion is similar to (14). An experimental determination of the reflection coefficient of ocean surface gravity waves on a natural beach in North Carolina [*Elgar et al.*, 1994] found values in good agreement with (14) and (15). From these simple considerations, we conclude that sea waves almost always break on beaches but may be reflected by cliffs. The locations of coastal DFM sources, which are found exclusively in front of steep rocky cliffs, indeed suggest that swell reflection plays an important role in the generation of DFM.

[42] During the experiment, spectral power varies over 2 orders of magnitude, which is significant but actually rather small. Indeed, this implies that the amplitudes of microseismic waves, which are proportional to the product between the amplitudes of the two opposite sea waves that produce them and the surface of the generation area [e.g., *Webb*, 1992], vary by a factor of only 10. These rather small source amplitude variations suggest that the fluctuations of the area of DFM sources are small, and that to first order they reflect the variations of significant wave heights in the generation area, which are also quite restricted (to a factor 3 at most), in good agreement with the results of *Bromirski et al.* [1999] and *Essen et al.* [2003]. Swell reflection tends to damp the variations of microseismic noise level by diminishing the amount of reflected swell when wave slope (or wave height) becomes so large that γ exceeds $\gamma_{\max}$, which may explain why energy variations of secondary microseisms are so small.

[43] While storms generate high waves over broad regions, the production of DFM seems to be concentrated inside very small areas. How can we explain this localization of DFM generation? *Longuet-Higgins* [1950] has proposed that the production of DFM is amplified by acoustic resonance inside the water layer when the wavelength of the compression wave in the water column is about a quarter of the ocean depth. To test this hypothesis,

we have determined the bathymetry at the locations of DFM sources and examined its hypsometric distribution (Figure 16, top). A pronounced maximum is indeed found around a depth of 2800 m. However, this maximum is also present in the distribution of bathymetry for the whole western Mediterranean basin, shown in Figure 16 (bottom). Unless fortuitous, this coincidence suggests that bathymetry plays a negligible role in the localization of DFM sources. Then, how can we explain the small extent of DFM sources compared to the very broad regions affected by storms? For coastal sources, the important parameter is probably the reflection coefficient of the swell. Reflection may be localized in a small region of the coast where the slope is particularly steep. Indeed, refraction of shoreward propagating gravity waves in shallow waters tends to rotate their propagation direction toward normal incidence. However, in waters deeper than half a wavelength, there is no refraction, and the reflection is specular. In this case, reflection will produce standing waves only where the coast is perpendicular to the incoming direction of the swell, which will strongly localize the sources of DFM.

[44] To explain the source locations in pelagic areas, we have to invoke other mechanisms. During the 17 December Mediterranean storm, the sources are first located west of Corsica, about 100 km off the coast. The wave model shows that in the region where we locate DFM sources, there is a strong interaction between waves from a nearby storm and the wind sea. These different contributions to the wave model are likely to have components in opposite directions, prone to interact and produce standing waves which will generate DFM. The day after, the wind rotates toward the west, the storm crosses the Mediterranean sea and reaches Menorca Island 8 h later. In less than 8 h, the storm center crosses a distance of about 300 km, with an average velocity of about 10.5 m/s, slightly larger than the group velocity of a 10-s gravity wave which from (5) is about 8 m/s. Thus waves are produced by the storm in front of the primary swell, a configuration that favors wave components propagating in opposite directions and generate DFM. Indeed, it should be possible to use the wave model to compute the amount of excitation by interaction of opposite waves. We will perform these calculations and compare them to our locations in a forthcoming study.

[45] Structural studies based upon the reconstruction of Green's functions from ambient noise have developed tremendously since the pioneering study of *Shapiro et al.* [2005]. Our study shows that the characteristic duration of dominant sources of DFM is typically a few days. To avoid biases in the reconstructed Green's functions, averages of the correlation functions should be done over time periods of at least a few weeks, thus limiting the temporal resolution in studies of time-dependent crustal properties.

6. Conclusion

[46] We have analyzed records of double-frequency microseisms to measure their incoming direction and amplitude at a number of stations in western Europe. Using this information, we are able to reconstruct the detailed spatio-temporal distribution of dominant sources of secondary microseisms in the Mediterranean Sea and in the North Atlantic Ocean. We have identified a small number of generation areas: the western coast of Corsica, the northern coast of Menorca Island, the northern Galicia margin and the western coast of Ireland. The position of these sources is remarkably stable in time but their excitation by storms in the Mediterranean Sea and in the Atlantic Ocean is episodic. Dispersion of apparent source location vectors is considerably reduced when we consider single stations, suggesting that locations are contaminated by small-scale crustal heterogeneities that deviate the waves off the great circle plane and that the generation area of DFM is rather limited in extent.

[47] We find evidence of both coastal and pelagic sources of DFM, suggesting that different mechanisms may produce standing waves in the ocean, and thus generate DFM. Swell reflection producing waves propagating in nearly opposite directions may explain the sources located close to the Galicia margin and to the western coast of Ireland. On the other hand, the deep water source locations probably result from a nonlinear interaction between primary swell and wind sea.

[48] With the set of stations used in the present study, we were not able to locate precisely the DFM sources in North Atlantic. In the future, we will add a number of stations in the British Isles and in northern Europe to constrain all the sources of DFM observed in western Europe. It will be also interesting to locate the sources of DFM during summer, which may be excited by different storm tracks, and characterize their seasonal variability.

[49] **Acknowledgments.** The Quercy array deployment would not have been possible without the support from local authorities and their help to find good installation sites. Our warmest thanks to all the landlords who hosted and took care of our instruments. Anne Paul allowed us to borrow recording stations and seismometers from the Lithoscope instrument pool, and Fabice Doré prepared and packaged the instruments. We thank Klaus Stammler for sending us the Gräfenberg array data. The paper benefitted from thoughtful reviews from the Associate Editor and two anonymous reviewers.

References

Bromirski, P. D., and F. K. Duennebier (2002), The near-coastal microseism spectrum: Spatial and temporal wave climate relationships, *J. Geophys. Res.*, *107*(B8), 2166, doi:10.1029/2001JB000265.
Bromirski, P. D., R. E. Flick, and N. Graham (1999), Ocean wave height determined from inland seismometer data: Implications for investigating wave climate changes in NE Pacific, *J. Geophys. Res.*, *104*, 20,753–20,766.
Cessaro, R. K. (1994), Sources of primary and secondary microseisms, *Bull. Seismol. Soc. Am.*, *84*, 142–148.
Donn, W. L., and B. Naini (1973), Sea wave origin of microbaroms and microseisms, *J. Geophys. Res.*, *78*, 4482–4488.
Elgar, S., T. H. C. Herbers, and R. T. Guza (1994), Reflection of ocean surface gravity waves from a natural beach, *J. Phys. Oceanogr.*, *102*, 8137–8157.
Essen, H., F. Krüger, T. Dahm, and I. Grevemeyer (2003), On the generation of secondary microseisms observed in northern and central Europe, *J. Geophys. Res.*, *108*(B10), 2506, doi:10.1029/2002JB002338.
Friedrich, A., F. Krüger, and K. Klinge (1998), Ocean-generated microseismic noise located with the Gräfenberg array, *J. Seismol.*, *2*, 47–64.
Garcés, M., M. Willis, C. Hetzer, A. Le Pichon, and D. Drob (2004), On using ocean swells for continuous infrasonic measurements of winds and temperature in the lower, middle, and upper atmosphere, *Geophys. Res. Lett.*, *31*, L19304, doi:10.1029/2004GL020696.
Grevemeyer, I., R. Herber, and H. H. Essen (2000), Microseismological evidence for a changing wave climate in the northeast Atlantic Ocean, *Nature*, *408*, 349–352.
Hasselmann, D. E., M. Dunckel, and J. A. Ewing (1980), Directional wave spectra observed during JONSWAP 1973, *J. Phys. Oceanogr.*, *10*, 1264–1280.
Hasselmann, K. (1963), A statistical analysis of the generation of microseisms, *Rev. Geophys.*, *1*, 177–210.

Haubrich, R. A., W. H. Munk, and F. E. Snodgrass (1963), Comparative spectra of microseims and swell, *Bull. Seismol. Soc. Am.*, *53*, 27–37.
Komen, G. J., L. Vavaleri, M. Donelan, K. Hasselmann, S. Hasselmann, and P. A. E. M. Janssen (1994), *Dynamics and Modelling of Ocean Waves*, Cambridge Univ. Press, New York.
Longuet-Higgins, M. S. (1950), A theory of the origin of microseisms, *Philos. Trans. R. Soc. London Ser. A.*, *243*, 1–36.
Miche, M. (1944), Mouvements ondulatoires de la mer en profondeur constante ou décroissante, *Annal. Ponts Chaussées*, *114*, 131–164.
Miche, M. (1951), Le pouvoir réfléchissant des ouvrages maritimes exposés à l'action de la houle, *Ann. Ponts Chaussées*, *121*, 285–319.
Munk, W., and M. Wimbush (1969), A rule of thumb for wave breaking over sloping beaches, *Oceanology*, *9*, 56–59.
Nikolaidis, N., and I. Pitas (1998), Nonlinear processing and analysis of angular signals, *IEEE Trans. Signal Process.*, *46*, 3181–3194.
Park, J., F. L. Vernon, and C. L. Lindberg (1987), Frequency dependent polarization analysis of high-frequency seismograms, *J. Geophys. Res.*, *92*, 12,664–12,674.
Pierson, W. J., and L. Moskowitz (1964), A proposed spectral form for fully developed wind seas based on the similarity theory of S. A. Kitaigorodskii, *J. Geophys. Res.*, *69*, 5181–5190.
Ponomaryov, E. A., A. G. Sorokin, and V. N. Tabulevich (1998), Microseisms and infrasound: A kind of remote sensing, *Phys. Earth Planet. Inter.*, *108*, 339–346.
Ramirez, J. M. (1940), An experimental investigation of the nature and origin of microseisms at St. Louis Missouri, *Bull. Seismol. Soc. Am.*, *30*, 35–84.
Schulte-Pelkum, V., P. S. Earle, and F. L. Vernon (2004), Strong directivity of ocean-generated seismic noise, *Geochem. Geophys. Geosyst.*, *5*, Q03004, doi:10.1029/2003GC000520.
Shapiro, N. M., M. Campillo, L. Stehly, and M. H. Ritzwoller (2005), High-resolution surface-wave tomography from ambient seismic noise, *Science*, *307*, 1615–1618.
Shemdin, K., K. V. Hasselmann, S. V. Hsiao, and K. Herterich (1978), Non linear and bottom interaction effects in shallow water, in *Turbulent Fluxes Through the Sea Surface, Wave Dynamics and Prediction*, edited by A. Favre and K. Hasselmann, pp. 347–372, Plenum, New York.
Stehly, L., M. Campillo, and N. M. Shapiro (2006), A study of the seismic noise from its long-range correlation properties, *J. Geophys. Res.*, *111*, B10306, doi:10.1029/2005JB004237.
Tabulevich, V. N., L. A. Drugova, and G. M. Troshina (1990), On observations of storm microseismic vibrations by seismic stations of the USSR, *Phys. Earth Planet. Inter.*, *63*, 209–218.
Tanimoto, T., S. Ishimaru, and C. Alvizuri (2006), Seasonality in particle motions of microseisms, *Geophys. J. Int.*, *166*, 253–266.
The Wamdi Group (1988), The WAM model—A third generation ocean wave prediction model, *J. Phys. Oceanogr.*, *18*, 1775–1810.
Webb, S. C. (1992), The equilibrium oceanic microseism spectrum, *J. Acoust. Soc. Am.*, *92*, 2141–2158.
Willis, M., M. Garcés, C. Hetzer, and S. Businger (2004), Infrasonic observations of open ocean swells in the Pacific: Deciphering the song of the sea, *Geophys. Res. Lett.*, *31*, L19303, doi:10.1029/2004GL020684.
Woodhouse, J. H., and Y. K. Wong (1986), Amplitude, phase and path anomalies of mantle waves, *Geophys. J. R. Astron. Soc.*, *87*, 753–773.

S. Benahmed, S. Chevrot, C. Ponsolles, and M. Sylvander, Dynamique Terrestrie et Planétaire, UMP 5562, Observatoire Midi-Pyrénés, Université Paul Sabatier, 14 Avenue Edouard Belin, F-31400 Toulouse, France. (chevrot@dtp.obs-mip.fr)

J. M. Lefèvre and D. Paradis, Météo-France, DPREVI/MAR, Marine and Oceanographic Section, 42 Avenue Coriolis, F-31057 Toulouse, France.